Stroboscopic *in situ* neutron diffraction approach to elucidate the kinetics of strain mechanisms in ferroelectric materials

Manuel Hinterstein,[1,2] Lucas Lemos da Silva,[1,2] Gaurav Vajpayee,[1,2] Kai-Yang Lee,[2] and Andrew Studer[3]
[1]*Fraunhofer IWM, 79111 Freiburg, Germany*
[2]*Institute of Applied Materials, Karlsruhe Institute of Technology, 76131 Karlsruhe, Germany*
[3]*Australian Nuclear Science and Technology Organisation, Sydney NSW 2234, Australia*

(Received 29 November 2022; accepted 21 February 2023; published 16 March 2023)

The electromechanical properties of ferroelectrics are often strongly frequency-dependent, but the underlying structural kinetics are not well known or understood. Here, we use *in situ* stroboscopic neutron diffraction combined with a comprehensive structural refinement method to examine the frequency-dependent structural change in the commercial actuator material PIC 151 at realistic operating frequencies. A broad range of frequencies was measured and analyzed in detail. This work further underlines the crucial role of the field-induced phase transformation for explaining the kinetics in ferroelectric materials. Both the tetragonal majority phase and the rhombohedral minority phase contribute with different effects to the frequency dependence of the strain mechanisms. Even creep effects well beyond the probed frequencies can be explained with the observations.

DOI: 10.1103/PhysRevMaterials.7.034406

I. INTRODUCTION

Ferroelectric actuators are used in a broad range of applications. These may require fast actuation, such as fuel injection, ink jet printers, or vibration damping, but also static positioning or slow movements, such as nanopositioning or drift corrections in monochromators, microscopes, or telescopes. Therefore, the kinetics of the strain mechanisms in ferroelectric actuator materials play a crucial role for the application on a broad range of frequencies. Since the materials and devices are usually operated without feedback, the macroscopic strain values should be ideally the same for a given electric field at any frequency. This is especially crucial for applications such as fuel injection, where actuation frequencies vary with engine speed. However, the literature reports various frequency-dependent effects on the poling of ferroelectrics [1,2].

A broad range of effects exists over a broad range of frequencies. This is reflected in the frequency-dependent behavior of the permittivity [3]. At high frequencies, only the displacement of electrons can be activated. By lowering the frequency, ionic displacements add to the permittivity. These frequencies are well into the THz regime [4]. By further reducing the frequency, domain-wall motions and domain switching can be accessed. These effects can be probed in the kHz to MHz regime with conventional impedance spectroscopy [5,6]. Finally, space charge zones and defect migration add contributions to the permittivity. Depending on the defect species, the corresponding frequencies can range from the Hz regime down to extremely low frequencies and might even be the origin of fatigue and degradation [7,8], which extend to time frames in the range of years. These dielectric effects are well known and can be studied with impedance spectroscopy and dielectric measurements.

When characterizing the electromechanical properties, several complex dynamic mechanisms have been reported. Dielectric studies focused on the polarization switching dynamics of lead zirconate titanate [$PbZr_xTi_{1-x}O_3$(PZT)] [2,9,10]. They found that the maximum polarization in PZT is always reached as long as the electric field exceeds values necessary to activate polarization switching. However, the switching time is strongly dependent on the applied electric field magnitude, the grain size, and the phase symmetry. These switching times might change by orders of magnitude, depending on the changed parameters. The investigation of polarization switching provides great insight into the material behavior and has already revealed the origin of electromechanical responses on long timescales. However, reports of time-dependent effects on the macroscopic strain are scarce. Zhou and Kamlah discovered a creep effect of the order of 10^2–10^3 s in a quasistatic experiment [11]. The effect could be reproduced in macroscopic experiments with effective frequencies of 16 μHz [12] and 50.5 μHz [13]. Such experiments are challenging due to drifts of temperature and components of the measurement equipment.

Such timescales are typical for *in situ* synchrotron or neutron measurements. We recently investigated the frequency range from μHz to mHz with *in situ* neutron and synchrotron experiments [12,14]. We analyzed the diffraction data with the STRAP method (Structure, Texture, and Rietveld Analysis for Piezoceramics). With this method, a quantitative analysis of all strain mechanisms is possible. The results revealed unprecedented details on the structural mechanisms of the macroscopic strain response. In particular, the fundamentally different behavior of the coexisting phases was previously unknown. While the tetragonal phase showed an unexpected decrease of unit-cell distortion with increasing field, the role of the rhombohedral phase is still unknown. The phase might either play an active role with intrinsic response to the electric

field, or be passively affected by the tetragonal domain switching, which imposes significant stresses on the surroundings.

In the past two decades, there has been strong debate over the PZT crystal structure with regard to the possible presence of a monoclinic phase at the morphotropic phase boundary [15]. The nature of this phase is still under debate. The monoclinic phase can continuously be interpreted from pseudotetragonal to pseudorhombohedral [16]. It might as well originate from coherence effects [17] or localized inhomogeneities [18]. For quantitative analysis methods such as the STRAP method, monoclinic phases result in extraordinarily large numbers of parameters due to the increased degrees of freedom. In the past, the macroscopic response to an applied electric field and even fundamental material parameters such as the piezoelectric coefficient could be correctly calculated from two-phase structure models with a tetragonal and a rhombohedral phase [12]. This indicates that at least some of the morphotropic compositions have rhombohedral or strongly pseudorhombohedral phases. Given that the refinement does not require a monoclinic phase to effectively model the data, the decision was made to focus on the kinetics of phases that are unambiguously present.

Since classic *in situ* synchrotron and spectroscopic neutron experiments usually operate in the frequency range from μHz to mHz [12,14], the results cannot be easily compared with macroscopic measurements and real applications. Therefore, STRAP analysis should be performed in realistic operating frequency ranges from mHz to Hz. Such frequencies are accessible with stroboscopic techniques for synchrotron [19] and neutron experiments [20]. However, extensive quantitative analysis, with stroboscopic data, over multiple frequency decades using the STRAP technique have not been performed to date.

Investigations into the switching kinetics of the electric-field-induced strain are more complex. Macroscopic measurements are compromised by overshooting and mechanical vibration in the experimental setup. Diffraction measurements may give direct structural insight but rely on techniques capable of matching the speed of switching. Using synchrotron radiation and a high frame-rate detector, Daniels, Cozzan, Ukritnukun, Tutuncu, Andrieux, Glaum, Dosch, Jo, and Jones revealed that the polarization reversal in PZT occurs through an intermediate domain orientation step, which results in a two-step reorientation process [21]. With stroboscopic diffraction methods, high frequencies can be accessed with scintillation detectors [22]. Such methods allow us to investigate the switching behavior on a range of solid solutions and enable us to characterize the electromechanical behavior for different frequencies on an atomic level [23,24]. For a lead-free material system, Schökel, Etter, Berghäuser, Horst, Lindackers, Whittle, Schmid, Acosta, Knapp, Ehrenberg, and Hinterstein were able to document a complex time structure during the rectangular and unipolar on-off switching at frequencies in the kHz range [19]. Here, the high angular resolution revealed a complex interaction of different coexisting phases.

Stroboscopic measurements are also possible with neutron diffraction. These rely on detectors that convert a detected neutron into a time-stamped electrical signal. Daniels, Finlayson, Studer, Hoffman, and Jones performed this for PZT at subcoercive fields of 1 Hz and could estimate the domain switching contributions [20]. Time-resolved and stroboscopic diffraction measurements are challenging for a range of reasons. To achieve good data quality with high statistics, all components of the experiment, such as the sample, beamline, detector, and electric field cycling, have to be rigorously adjusted. Therefore, most studies focus on single reflection analysis or phenomenological characterizations [25]. In contrast, recently, Lee, Shi, Kumar, Hoffman, Etter, Checcia, Winter, Lemos da Silva, Seifert, and Hinterstein were able to quantitatively analyze stroboscopic synchrotron diffraction measurements with the STRAP method [26]. Here, in a lead-free composition, the complex strain mechanisms of coexisting phases could be revealed and correlated with the macroscopic behavior. Most of the modern beamlines at synchrotron or neutron facilities measure a broad range in 2θ with either 2D detectors [27–29] or 1D detectors [30,31], and even 0D scintillation detectors are usually designed as multianalyzer detectors [19,32,33]. Therefore, a full pattern analysis such as the STRAP method is able to exploit the full range of measured information.

Since the kinetic effects of the macroscopic strain and their underlying structural mechanisms are still not well understood, we performed stroboscopic *in situ* neutron diffraction experiments with a technically applied PZT material (PIC 151) under realistic operating frequencies. Using the STRAP method on stroboscopic neutron data, we reveal details of the crystal structure and the strain mechanisms. The results help us to understand the electromechanical behavior on a broad range of frequencies and will help to not only tailor the properties of existing materials, but also to develop future lead-free actuator materials with frequency-independent properties.

II. EXPERIMENT

Sintered samples of the technologically applied actuator material PIC 151 ($Pb_{0.99}[Zr_{0.45}Ti_{0.47}(Ni_{0.33}Sb_{0.67})_{0.08}]O_3$, PI Ceramics, Lederhose, Germany) [34] were cut and polished into rectangular bars of dimension $3.5\times3.5\times25$ mm. Platinum electrodes with a thickness of approximately 50 nm were sputtered on two opposing long sides of the samples. Neutron-diffraction data were collected at the Wombat beamline of the Australian Nuclear Science and Technology Organization (ANSTO) in Sydney, Australia [35]. The STRAP measurement strategy for neutron diffraction entails the measurement of a sample with the applied field direction in the diffraction plane [Fig. 1(a)]. The sample orientation is changed by an ω-rotation, and full diffraction patterns are measured for each orientation of the electric-field direction. This orientation series leads to data that allow a direct observation of the strain mechanisms. The detector at the wombat beamline delivers a quasi-2D diffraction pattern, which can be reduced to 1D-diffraction patterns by either radially integrating up all the data along the detector width χ or by slicing along χ in intervals. The resulting orientation series can be used for the STRAP method and show the characteristic lattice strain for the 111 reflection, as well as texturing and phase transformation for the 200 reflections as depicted in Fig. 1(b).

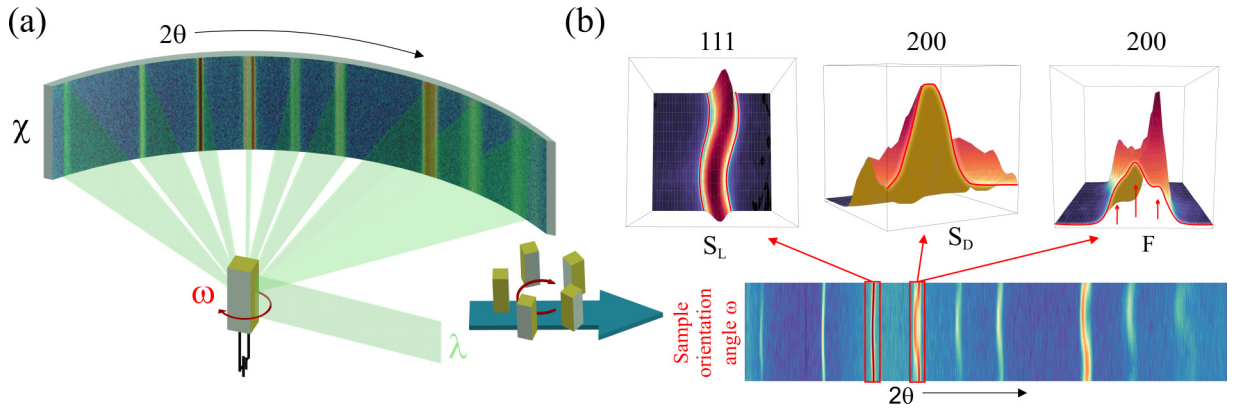

FIG. 1. (a) Measurement setup for a single orientation during *in situ* measurement with neutrons. (b) Integrated orientation series with magnifications of the characteristic 111 and 200 reflections, where lattice strain (S_L), domain switching strain (S_D), and phase fractions (F) are indicated with red lines and arrows.

The samples were continuously cycled with a bipolar electric field, and orientation series of diffraction patterns were measured at two wavelengths. A shorter wavelength of $\lambda = 1.63$ Å was used for a large Q-range and a longer wavelength of $\lambda = 2.41$ Å for high angular resolution. The electric field was applied in a special *in situ* sample environment for applying high electric fields [28]. For stroboscopic measurements, the sample is cycled with an electric field of a periodic waveform, and data are collected with the detector being triggered by the electric-field cycling. Details can be found elsewhere [25]. The continuous cycling frequency was generated by an Agilent 33250A waveform generator. The waveform generator was coupled with a TREK 20/20C high-voltage amplifier and synchronized with the detector in order to control the stroboscopic measurements.

Cyclic electric fields with an amplitude of 2 kV/mm were applied as a stepped triangular wave, with ten steps ascending and descending, as described previously [28]. The cycling frequencies were 100 mHz, 1 Hz, 10 Hz, and 100 Hz. For each frequency and each wavelength, a sample rotation series of 12 angular ω orientations was measured. Stroboscopic data were summed up in 160 bins and later binned to the 20 electric-field steps. This resulted in a six-dimensional experiment of wavelength, 2θ, intensity, sample orientation, electric field (time), and frequency. An additional cycling experiment with the same degrees of freedom at 250 Hz was performed with unipolar on-off (square wave) switching. Here the full 160 bins were used for analysis without rebinning.

Rietveld refinement was performed using the software package MAUD (Materials Analysis Using Diffraction) [36] with a tetragonal $P4mm$ and a rhombohedral $R3m$ phase, since this two-phase model could successfully describe the structure of PIC 151 [12,14]. The exact details of the experiment and refinement of the STRAP method can be found elsewhere [14]. With data of an unpoled sample, atomic positions and microstructural parameters such as crystallite size and microstrain were refined. These values were kept fixed during the refinements with the *in situ* data. For the refinements with the *in situ* data, a parameter set of lattice parameters, texture, and strain were refined. Additionally scale parameters accounted for the phase fractions and overall intensity. The background was interpolated between background points in nonoverlapping regions, and a general background parameter accounted for the background level. Direct macroscopic measurements, which were used to compare with STRAP-derived values, were taken with an aixACCT TF analyzer (TF1000, aixACCT, Germany). In continuous mode, frequencies from 100 mHz to 100 Hz were accessible.

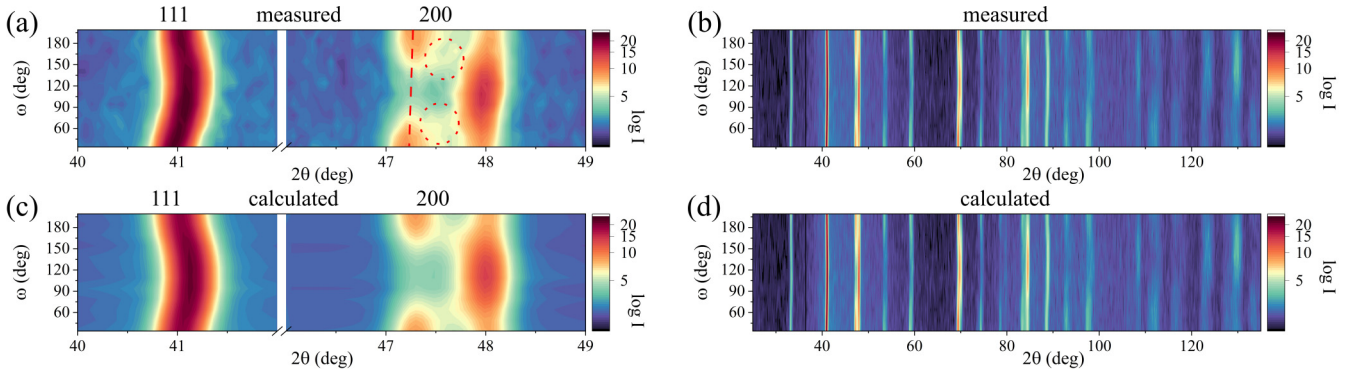

FIG. 2. STRAP-refinement with the orientation series data, measured at 1.63 Å with 1 Hz in the remanent state at 0 kV/mm. (a), (c) Magnification of the 111 and 200 reflections, and (b), (d) full diffraction patterns. Intensities are plotted on a logarithmic scale.

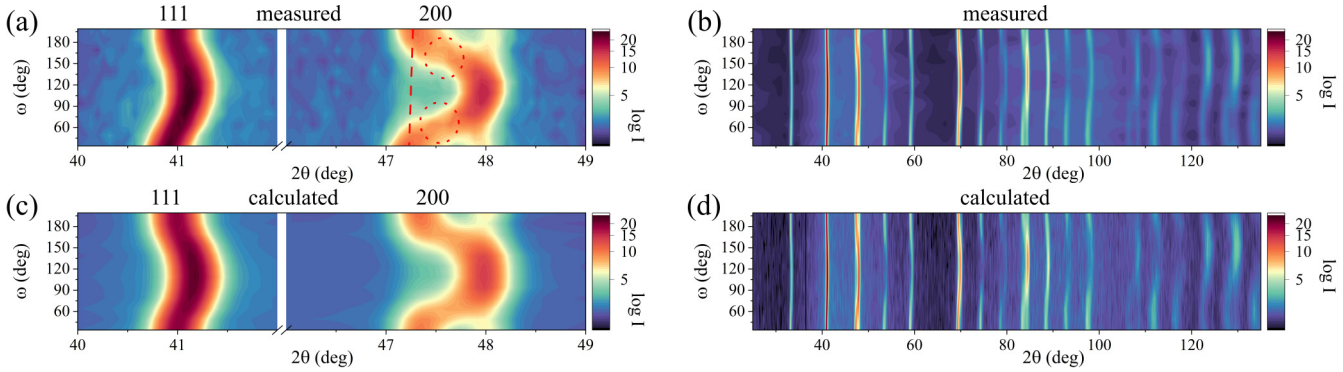

FIG. 3. STRAP-refinement with the orientation series data, measured at 1.63 Å with 1 Hz in the applied field state at 2 kV/mm. (a), (c) Magnification of the 111 and 200 reflections, and (b), (d) full diffraction patterns. Intensities are plotted on a logarithmic scale.

III. RESULTS AND DISCUSSION

To study the kinetic effects, we performed stroboscopic neutron diffraction at the Wombat beamline at ANSTO. The information was maximized by collecting full powder patterns over a broad orientation range at two wavelengths of 1.63 and 2.41 Å. With 2.41 Å, maximum angular resolution for the low indexed reflections can be achieved. With 1.63 Å, a high Q-range is accessible. By combining both measurements, a STRAP refinement of high quality is possible [14]. The results for 1.63 Å at 1 Hz are shown in Fig. 2 for the remanent state at 0 kV/mm and in Fig. 3 for the applied field state at 2 KV/mm. The results for 2.41 Å at 1 Hz are shown in Fig. 4 for the remanent state at 0 kV/mm and in Fig. 5 for the applied field state at 2 KV/mm.

The full pattern comparison of parts (b) and (d) in Figs. 2–5 demonstrates the high level of agreement between the measured and the calculated diffraction patterns of the STRAP refinement. The magnifications of the 111 and 200 reflections again show the extraordinarily high agreement of measured and calculated diffraction patterns. While in the remanent state the 200 reflections are clearly separated [Figs. 2 and 4, parts (a) and (c)], the 200 reflections are connected with intermediate intensities in the applied field state [Figs. 3 and 5, parts (a) and (c)]. These intermediate intensities can be misinterpreted as strong orientation-dependent reflection shift. However, the actual origin of these intensities is an orientation-dependent phase transformation from the tetragonal to the rhombohedral phase as already outlined in earlier studies [12,14]. The effect is well resolved in the measurements and relatively strong at this frequency of 1 Hz.

The change of intensities in the 200 reflections between the remanent and the applied field state is challenging to assess just from the depicted representation. However, in order to visualize all reflections, a logarithmic intensity scale was applied. The domain switching is visible in the 200 reflections as a change in intensity along the sample orientation angle. The phase transformation is visible as additional intensity in between the 200 reflections for special sample orientation angles. Compared to the phase transformation [red circles in Figs. 2(a), 3(a), 4(a), and 5(a)], the change of the domain switching [red lines in Figs. 2(a), 3(a), 4(a), and 5(a)] appears to be less pronounced. The reflection shift of the 111 reflection is clearly visible in the remanent state, indicating a remanent strain from lattice strain, and it increases in the applied field state.

The quantitative STRAP analysis allows us to calculate the macroscopic response of the material from the obtained structural information [12,14]. Apart from detailed crystal structure information on the individual phases, this yields the phase fractions F_T and F_R, the lattice strain $S_{L,T}$ and $S_{L,R}$, and the domain switching strain $S_{D,T}$ and $S_{D,R}$. Details on the calculations of the individual components were described in

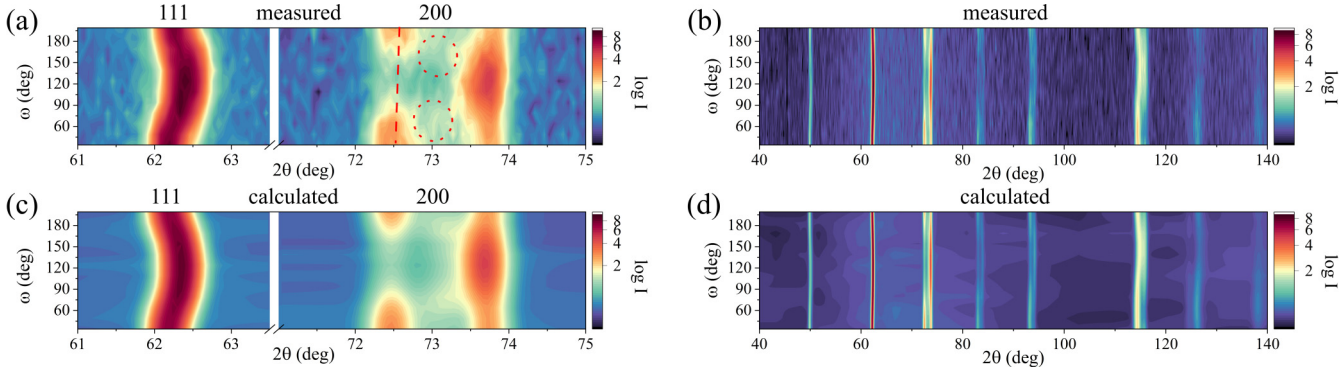

FIG. 4. STRAP-refinement with the orientation series data, measured at 2.41 Å with 1 Hz in the remanent state at 0 kV/mm. (a), (c) Magnification of the 111 and 200 reflections, and (b), (d) full diffraction patterns. Intensities are plotted on a logarithmic scale.

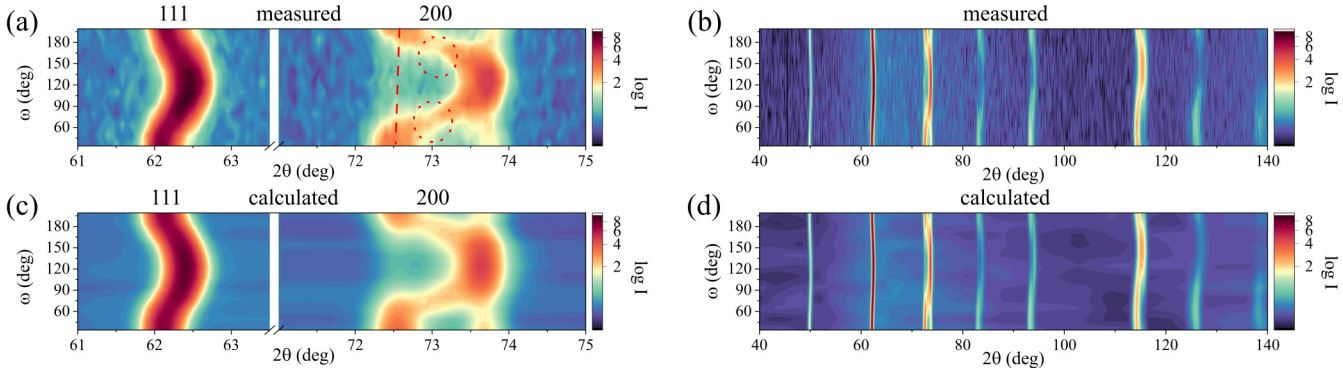

FIG. 5. STRAP-refinement with the orientation series data, measured at 2.41 Å with 1 Hz in the applied field state at 2 kV/mm. (a), (c) Magnification of the 111 and 200 reflections, and (b), (d) full diffraction patterns. Intensities are plotted on a logarithmic scale.

previous studies [12,14]. From this information, the macroscopic strain S can be calculated:

$$S = F_T(S_{L,T} + S_{D,T}) + F_R(S_{L,R} + S_{D,R}).$$

Figure 6(a) shows the electric-field-induced strain, calculated from diffraction by the STRAP method [12] for different unipolar frequencies. Compared to macroscopic measurements [Fig. 6(b)], the unipolar strain loops show significantly less hysteresis. This might be due to the free-standing geometry in the *in situ* setup [28]. This difference in strain behavior was observed previously [26]. The hysteresis loops all show the same behavior and magnitude, except the data from the sample measured at 100 mHz. Here the overall strain level is slightly higher. This was explained earlier by creep in this material [11]. In general, the calculated hysteresis loops show the expected behavior and again prove the validity of the STRAP method.

The frequency dependence of the tetragonal phase fraction is plotted in Fig. 7(a). The hysteresis loops look broadly the same: with increasing electric field, the tetragonal phase fraction decreases from the remanent value. This indicates the electric-field-induced transformation to the rhombohedral phase, observed already in the literature [12,14]. With increasing frequency, the hysteresis loops shift to higher tetragonal phase fraction. The values at the remanent and maximum applied field are shown in Fig. 7(b). At the same time, the change in phase fraction between the two extremes stays constant at around 20%. This is in contrast to the calculated strain loops from Fig. 6, where the frequency difference is less pronounced.

A more detailed investigation of the structural changes in the individual phases is possible with the unit-cell distortion η. This describes the deviation from cubic symmetry and is defined as

$$\eta_T = \frac{c_T}{a_T} - 1$$

for the tetragonal phase and as

$$\eta_R = \frac{\sqrt{2}c_H}{\sqrt{3}a_H} - 1$$

for the rhombohedral phase. The index H denotes the hexagonal setup of the unit cell for the rhombohedral phase.

A similar behavior to that for the phase fractions can be observed for the unit-cell distortions η_T and η_R [Fig. 8(a)]. Here, η_T decreases with electric field, which was already reported [12]. This is in contrast to the classic model for the converse piezoelectric effect. In the classic model of the converse piezoelectric effect, when an electric field is applied,

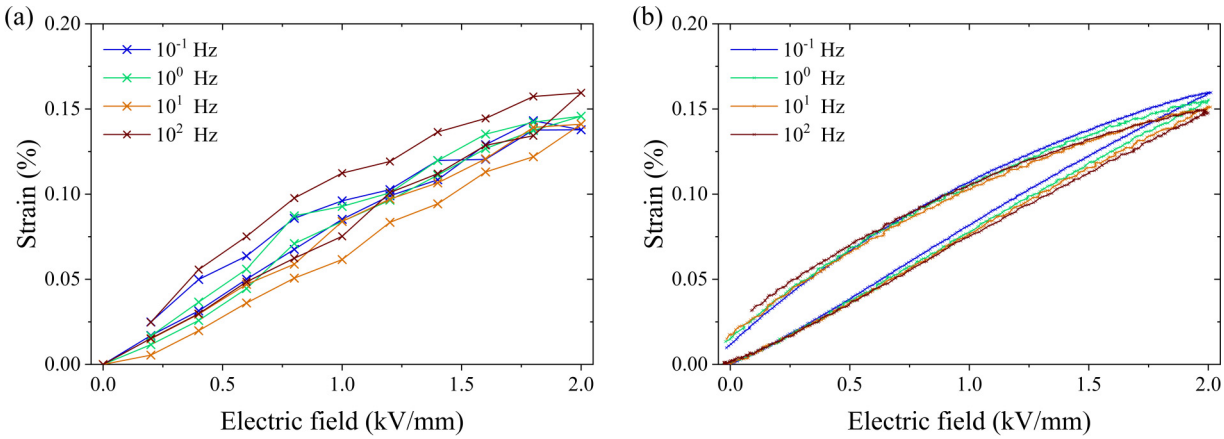

FIG. 6. Electric-field-induced unipolar strain, (a) calculated from diffraction by STRAP [12] and (b) macroscopically measured with a TF analyzer for different frequencies.

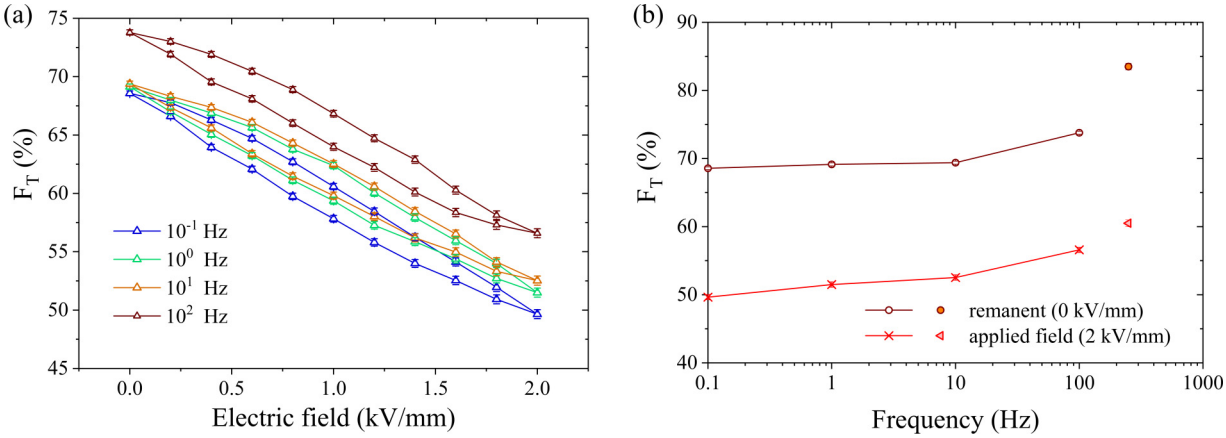

FIG. 7. (a) Tetragonal phase fraction as a function of electric field for different frequencies and (b) remanent and applied field values of the tetragonal phase fractions as a function of frequency. Phase fractions from 0.1 to 100 Hz are derived from the hysteresis loops of Fig. 2(a). The phase fraction at 250 Hz is derived from the final on-off field measurement.

the unit cell expands along the polarization direction, increasing the unit-cell distortion and the spontaneous polarization. In a material such as PIC 151 with $\eta_T \approx 1.5\%$, the behavior is opposite. Due to the field-induced domain switching, the switched c-axis will be shorter and thus the overall average unit-cell distortion decreases with increasing electric field. For the rhombohedral phase, η_R is slightly increasing with electric field. This occurs due to the significantly lower distortion of around 0.4%, which is in the range of the overall electric-field-induced strain. In the rhombohedral case, the classic model of the converse piezoelectric effect applies and η_R increases with electric field.

Figure 8(b) again shows a continuous trend with increasing frequency, similar to the tetragonal phase fraction. However, for the unit-cell distortion, the overall trend points towards a decreasing unit-cell distortion. This indicates that during domain switching, the precipitation of the resulting unit-cell distortion exhibits kinetics down to the low Hz range. The earlier described creep effects, therefore, appear to be connected to the field-induced phase transformation and the domain switching. During the significant change of the phase composition and the domain configurations, the resulting stress-strain effects and intergranular stresses [37] readjust with kinetics on a broad range of timescales.

To further investigate the kinetics at high frequencies, we performed a unipolar stroboscopic on-off experiment at 250 Hz with 2 kV/mm. At this frequency, the tetragonal phase fraction decreases to around 60.5% in the applied field state at 2 kV/mm and reaches around 83.5% in the remanent state. The values of this experiment are included in Fig. 7(b). The trend of the phase fractions as a function of frequency in Fig. 7(b) shows a similar behavior to that of the lattice parameters previously reported for a lead-free material [25]. That work reported an exponential proportionality of the lattice parameter with the frequency $a_C \sim f^p$. Since the morphotropic phase boundary in PZT is slightly tilted [16], an increase in temperature results in an increase in tetragonal phase fraction. Therefore, the trend indicates that at higher frequencies the material is self-heating due to the significant switching processes from extrinsic contributions like domain switching [38]. We already observed such a behavior for a frequency of 100 Hz in a lead-free composition [25]. A temperature increase can also be anticipated from the trend of the unit-cell distortions in Fig. 8(b). While $\Delta\eta_T$ is constant

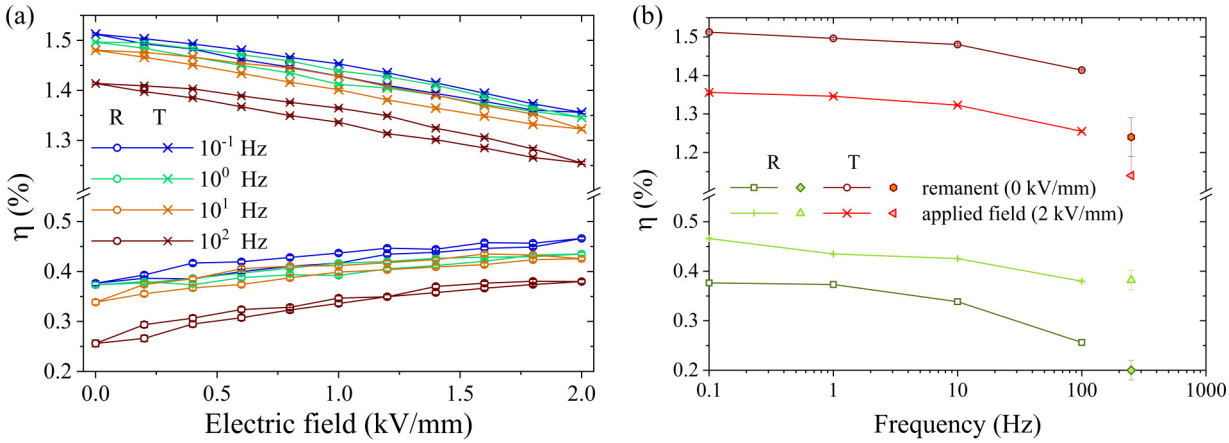

FIG. 8. Unit-cell distortion η of the tetragonal and the rhombohedral phase as a function of (a) electric field and (b) remanent and applied field values of the unit-cell distortions as a function of the frequency. Values at 250 Hz are derived from the final on-off switching experiment.

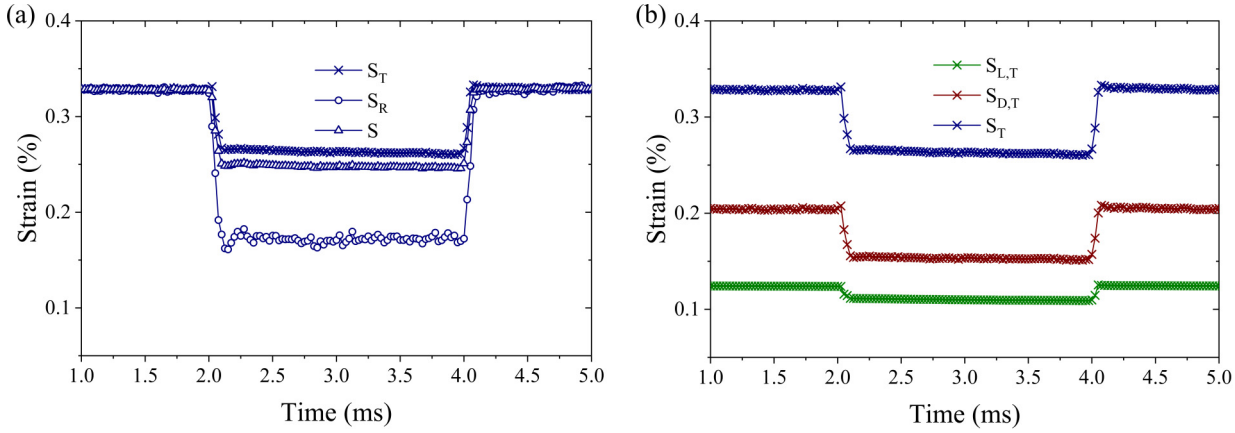

FIG. 9. (a) Electric-field-induced strain of the tetragonal (S_T) and rhombohedral (S_R) phase together with the overall strain (S) as a function of time during a rectangular on-off cycling with 250 Hz and 2 kV/mm. (b) The tetragonal strain and its individual components lattice strain ($S_{L,T}$) and domain switching strain ($S_{D,T}$).

up to 100 Hz for triangular waveforms, it significantly decreases for the rectangular waveform and 250 Hz. Also, the overall values decrease significantly, which again indicates an increased temperature. Interestingly η_R follows the trend of the triangular waveforms. Here $\Delta\eta_R$ continuously increases and the trend of η_R is not affected by increasing the frequency and changing the waveform.

Figure 9(a) shows the overall electric-field-induced macroscopic strain and the contributions to the strain from each phase, calculated from diffraction by the STRAP method. Since the tetragonal phase fraction dramatically increased for the rectangular waveform, the tetragonal strain S_T dominates the overall strain behavior, and the rhombohedral strain is rather noisy due to the low phase fraction. Details of the tetragonal phase are plotted in Fig. 9(b). Due to the still high unit-cell distortion of 1.1–1.3 %, the domain switching strain $S_{D,T}$ dominates the tetragonal strain. The change in lattice strain is comparably small.

By using an on-off square wave, it becomes possible to investigate the structural kinetics during the 2 ms hold time of the remanent and applied field states. Since the time-dependent changes are small, they are not clearly visible in Fig. 9. For a better visualization, the changes in strain have to be plotted as a function of time in the respective interval. Figure 10 shows 2 ms of the remanent and applied field intervals, with the strain scaled relative to the initial value. At around -0.005%, the changes in strain during the hold state are about an order of magnitude smaller than the electric-field-induced changes. Interestingly, the changes in both cases are negative. This indicates a further relaxation towards lower strain in both the applied field and the remanent state. In the applied field state at 2 kV/mm, the lattice strain $S_{L,T}$ continuously relaxes without any indication of a saturation by about -0.001% in the 2 ms interval. The domain switching strain $S_{D,T}$ shows significantly more noise. This is due to the calculation method of $S_{D,T}$, which involves a range of refined parameters [14]. Here the time-dependent values decrease more quickly and appear to saturate after around 1.5 ms at around -0.003%.

In the remanent state at 0 kV/mm [Fig. 10(b)], $S_{L,T}$ decreases more rapidly and oscillations appear. A saturation might occur at around 3.5 ms and -0.002%. $S_{D,T}$ decays at a very similar rate to $S_{L,T}$ and also shows similar oscillations, and a saturation might occur at around 3.5 ms at around -0.003%. The relaxation in the remanent state appears in general more pronounced and more equally distributed between $S_{L,T}$ and $S_{D,T}$. Additionally, both strain mechanisms seem to have a continuously decreasing trend far beyond the timescale probed in this experiment. Interestingly, the strains in both states decrease over time with no indication of the positive creep described in the literature, which leads to increased strain at low frequencies [11]. However, since the decrease in the applied field state is smaller than in the remanent state, and this trend seems to extend to longer timescales, this might be the explanation why the strain amplitude increases for lower frequencies as shown in Fig. 7(b).

In contrast, the phase fractions follow a different trend as shown in Figs. 11(a) and 11(b). When the field is applied, F_T decreases as already discussed for lower frequencies and the triangular waveform in the context of Fig. 7. However, the initial value reached is around 61.5% [Fig. 11(a)]. Within the following 2 ms, F_T decreases and asymptotically reaches 60.5%. When the field is removed, F_T sharply increases to around 83%. In the following 2 ms, F_T continuously increases with no indication of saturation. Therefore, the asymptotic behavior in the applied field state and the behavior of a continuous increase in the remanent state is similar for the strain mechanisms and the phase fractions. This indicates that the structure stabilizes faster under the influence of an applied field than in the field-free state.

Figure 12(a) shows the rhombohedral strain mechanisms during the 250 Hz rectangular cycling. Due to the low phase fraction, the noise is significantly higher, especially for the domain switching strain. Other than in previous studies reported [12,14], here also the rhombohedral strain mechanisms are dominated by domain switching. However, compared to Fig. 9(b), $S_{D,R} < S_{D,T}$ and $S_{L,R} > S_{L,T}$. When the field is removed, $S_{D,R}$ sharply decreases and shows a spike while approaching the low values [red circle, Fig. 12(a)]. Since S_D is proportional to η, a closer look at the unit-cell distortion reveals that a similar behavior appears for η_R [red circle, Fig. 12(b)]. F_R, on the other hand, exhibits a spike during field application [blue circle, Fig. 12(b)]. This behavior

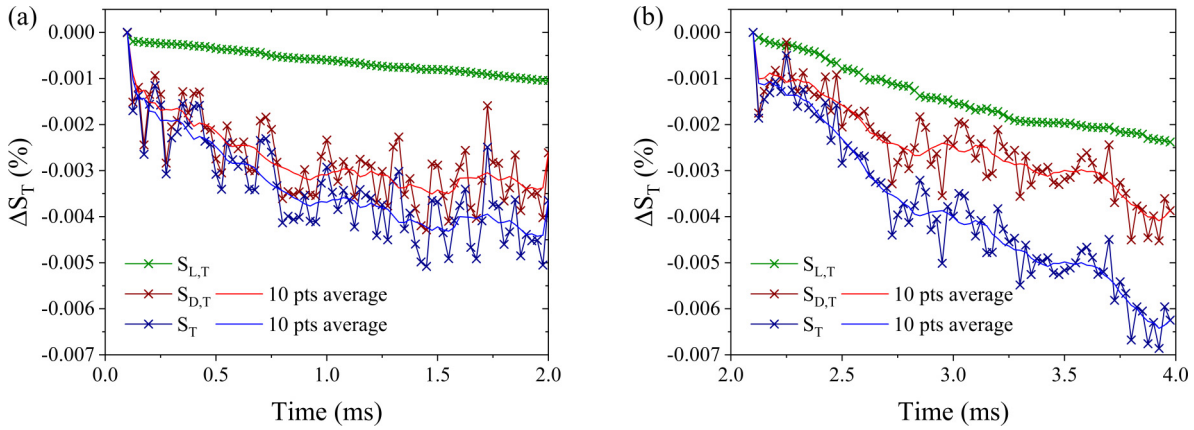

FIG. 10. Changes in the strain contributions as a function of time during the 250 Hz rectangular unipolar cycling at (a) the applied field state at 2 kV/mm and (b) the remanent state at 0 kV/mm.

indicates that the rhombohedral phase accommodates stresses during switching and acts as a buffer between the tetragonal switching grains. Since the tetragonal phase exhibits such a large unit-cell distortion, the tetragonal domain switching induces stresses in the surrounding microstructure. These stresses affect the rhombohedral phase during both the on and off switching of the electric field. The rhombohedral phase accommodates the stresses during the few hundred μs of the spikes.

Previous results from the STRAP method on the same material revealed dramatic differences in the electric-field-dependent behavior of the two phases [12,14]. However, it was unclear why especially the rhombohedral minority phase exhibits such a strong response, especially at the coercive field. In general, the rhombohedral phase in PIC 151 exhibits a strong lattice strain and weak domain switching. The weak domain switching can be explained by the low rhombohedral unit-cell distortion [Fig. 8(a)]. However, the strong lattice strain can be explained in two ways:

(i) The explanation of active behavior assumes a strong intrinsic response of the rhombohedral phase to the applied electric field. This model emanates from an active response of the phase to the external stimulus. The model for explaining the strong lattice strain involves the converse piezoelectric effect as the main driving force in the rhombohedral phase.

(ii) The explanation of passive behavior considers the large unit-cell distortion of the tetragonal phase. As can be seen in Fig. 8(a), η_T continuously decreases with increasing field. This occurs due to the large distortion, which results in a smaller switched c-axis than in the remanent state. Since the STRAP method determines just a single set of lattice parameters for each phase, the averaging of the diffraction experiment results in a decreasing unit-cell distortion with increasing field. The reason is the increasing volume fraction of switched domains [39]. This model already accounts for the large stresses due to the tetragonal domain switching. These stresses could also affect the coexisting phase and deform it during the switching process. Such a stress accommodating minority phase has already been reported in a lead-free material [40].

The results presented in this work can be used to elucidate whether the rhombohedral phase responds in an active or a passive way. In this context, active refers to an intrinsic response of the phase to the applied electric field. When using the example of the classic model of the converse piezoelectric effect, active would mean that with an applied electric field the

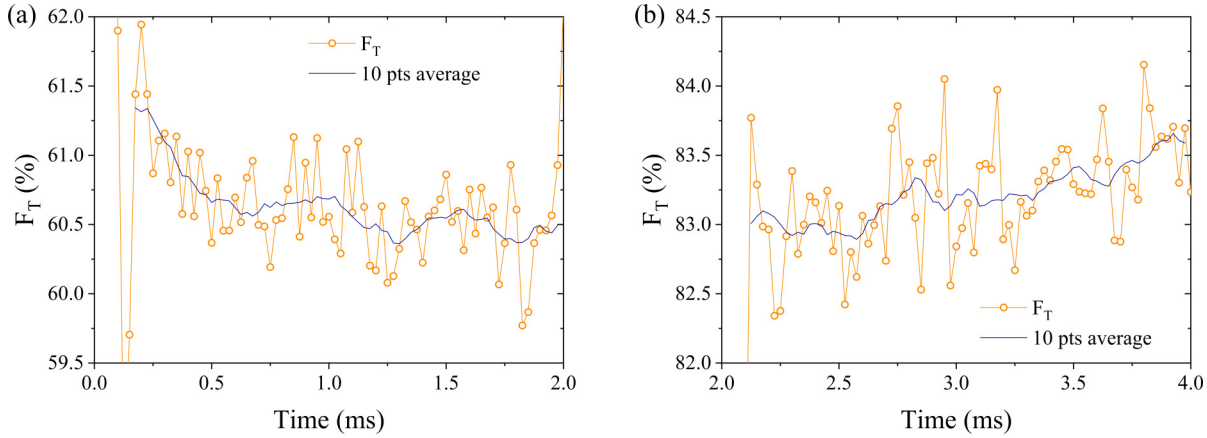

FIG. 11. Changes in tetragonal phase fractions as a function of time during the 250 Hz rectangular unipolar cycling during (a) the applied field state at 2 kV/mm and (b) the remanent state at 0 kV/mm.

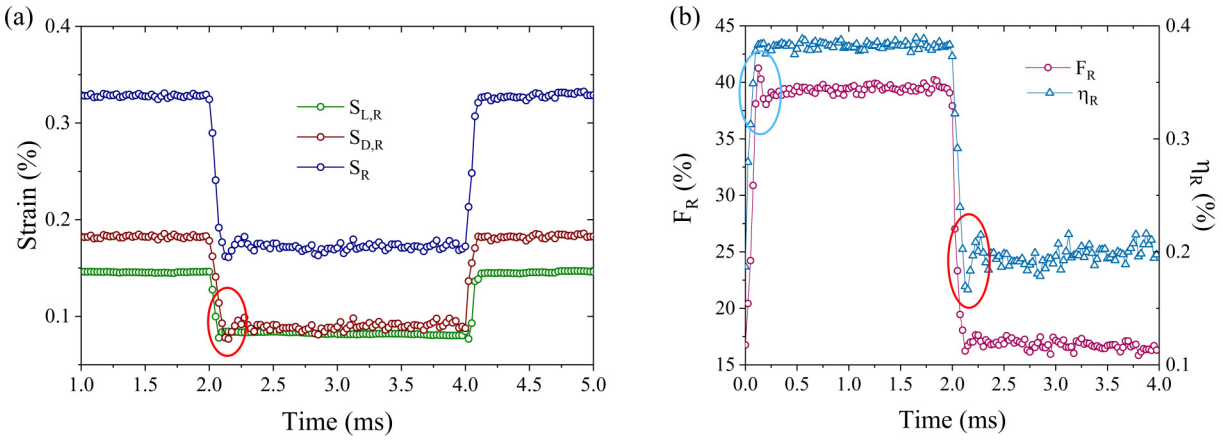

FIG. 12. Strain mechanisms of the rhombohedral phase as a function of time during the 250 Hz rectangular unipolar cycling.

unit cell expands due to the spontaneous polarization responding to the external stimuli. Passive, on the other hand, refers to external effects leading to the observation. One possibility, again for the example of the converse piezoelectric effect, would be the domain switching of the tetragonal phase. Since the tetragonal phase exhibits a significantly larger unit-cell distortion, domain switching leads to substantial stresses in the surrounding microstructure. A grain that is dominated by tetragonal domain switching could impose stresses on a neighboring grain which is dominated by rhombohedral symmetry. This would also lead to an increase of rhombohedral unit-cell distortion.

The spikes in Fig. 12 indicate that during switching, elastic mechanical processes are activated. These are just indirectly visible through the spikes in F_R and η_R. When the field is applied to PIC 151, a field-induced phase transformation to a rhombohedral phase occurs. The immediate electric-field application results in an overshoot of F_R by about 3% for about 100 μs. When the field is removed, the rhombohedral unit-cell distortion η_R decreases and creates a similar effect on a similar timescale. These mechanisms indicate an elastic mechanical behavior and can directly be related to the fatigue effects reported in PIC 151 [7]. Even though the electric field induces a phase transformation towards the rhombohedral phase, cycling for 10^7 cycles results in a more tetragonal structure. This indicates that PIC 151 possesses a unique pinning of the initial structural features. The initial structure is predominantly tetragonal in PIC 151. Therefore, the interatomic potentials which define the atomic distances promote tetragonal symmetry. We could show this in a previous study, where the tetragonal lattice parameters of PIC 151 in the unpoled state have exactly the same values as in the remanent state [12]. For the rhombohedral phase, the unit-cell parameters of the unpoled state deviate significantly from the remanent state. This indicates a constant stress state. When the field is applied, the rhombohedral phase is induced, but when the field is removed, the interatomic potentials pull the structure back to tetragonal symmetry. Thus, the tetragonal structure is pinned by the interatomic potentials. This behavior results in a reversible switching between the symmetries and is a key property for high electric-field-induced strain.

From the results, an active or passive behavior cannot be unambiguously concluded. However, the fact that the spikes are observed for the rhombohedral phase and can be linked with stresses originating from the tetragonal phase indicates a passive behavior of this phase. Obviously, the unique properties of lead-based ferroelectric materials are based on the extraordinary structural mechanisms underlying the electromechanical response. The results reported here reveal yet another detail and will help to better understand the strain mechanisms in ferroelectrics. This knowledge allows us to create guidelines to develop as well as tailor new sustainable materials.

IV. CONCLUSION

Our results from a broad range of frequencies provide detailed insight into the kinetics of electric-field-induced strain mechanisms in ferroelectric materials. In particular, the role of the field-induced phase transformation could be elucidated. The already known creep effects on the low end of applied frequencies are coupled with domain switching of the tetragonal majority phase and the field-induced phase transformation.

A high-frequency switching experiment revealed kinetic effects in the range of μs to ms. All analyzed strain mechanisms showed drifting behavior in the applied field state as well as the remanent state. However, the drift in the applied field state is smaller than in the remanent state, and this trend seems to extend to longer timescales. This explains very well why the strain amplitude increases for lower frequencies and thus ultimately the quasistatic creep effects.

Our results further indicate that the structure stabilizes faster under the influence of an applied field than in the field-free state. This again leads to an explanation for the increased strain at low frequencies or quasistatic conditions. Apart from the directly observable effects in the tetragonal majority phase, the phase transformation and thus the rhombohedral minority phase play crucial roles as well. Due to the averaging character of the diffraction experiments, the behavior of the rhombohedral phase can be explained either with an active or a passive character. The most likely scenario, however, is a passive behavior where the rhombohedral phase accommodates stresses during switching and acts as a buffer between the tetragonal switching grains.

ACKNOWLEDGMENTS

The authors thank the Deutsche Forschungsgemeinschaft (DFG) under Grant No. 1867/1-2 and the Fraunhofer Internal Programs under Grant No. Attract 40-04857 for financial support. The authors thank the Australian Nuclear Science and Technology Organisation for beamtime at the Wombat beamline under program proposal PP4304.

[1] S. Zhukov, M. Acosta, Y. A. Genenko, and H. von Seggern, Polarization dynamics variation across the temperature- and composition-driven phase transitions in the lead-free $Ba(Zr_{0.2}Ti_{0.8})O_{3-x}(Ba_{0.7}Ca_{0.3})TiO_3$ ferroelectrics, J. Appl. Phys. **118**, 134104 (2015).

[2] S. Zhukov, Y. A. Genenko, O. Hirsch, J. Glaum, T. Granzow, and H. von Seggern, Dynamics of polarization reversal in virgin and fatigued ferroelectric ceramics by inhomogeneous field mechanism, Phys. Rev. B **82**, 014109 (2010).

[3] A. K. Bain and P. Chand, *Ferroelectrics* (Wiley-VCH, Weinheim, 2017).

[4] R. Dorey, Microstructure-property relationships, in *Ceramic Thick Films for MEMS and Microdevices* (Elsevier, Amsterdam, 2012), pp. 85–112.

[5] G. Picht, N. H. Khansur, K. G. Webber, H. Kungl, M. J. Hoffmann, and M. Hinterstein, Grain size effects in donor doped lead zirconate titanate ceramics, J. Appl. Phys. **128**, 214105 (2020).

[6] G. Helke and K. Lubitz, *Piezoelectric PZT Ceramics, in Piezoelectricity* (Springer, Berlin, 2008), pp. 89–130.

[7] M. Hinterstein, J. Rouquette, J. Haines, P. Papet, J. Glaum, M. Knapp, J. Eckert, and M. Hoffman, Structural contribution to the ferroelectric fatigue in lead zirconate titanate ceramics, Phys. Rev. B **90**, 094113 (2014).

[8] Y. a. Genenko, J. Glaum, M. J. Hoffmann, and K. Albe, Mechanisms of aging and fatigue in ferroelectrics, Mater. Sci. Eng. B **192**, 52 (2015).

[9] S. Zhukov, H. Kungl, Y. A. Genenko, and H. von Seggern, Statistical electric field and switching time distributions in PZT 1Nb2Sr ceramics: Crystal- and microstructure effects, J. Appl. Phys. **115**, 014103 (2014).

[10] S. Zhukov, Y. A. Genenko, and H. von Seggern, Experimental and theoretical investigation on polarization reversal in unfatigued lead-zirconate-titanate ceramic, J. Appl. Phys. **108**, 014106 (2010).

[11] D. Zhou and M. Kamlah, Room-temperature creep of soft PZT under static electrical and compressive stress loading, Acta Mater. **54**, 1389 (2006).

[12] M. Hinterstein, K.-Y. Lee, S. Esslinger, J. Glaum, A. J. Studer, M. Hoffman, and M. J. Hoffmann, Determining fundamental properties from diffraction: Electric field induced strain and piezoelectric coefficient, Phys. Rev. B **99**, 174107 (2019).

[13] S. Eßlinger, P. Neumeister, A. Schönecker, M. Hoffman, A. Studer, and M. Hinterstein, In situ neutron diffraction studies on poling of the Hard PZT Ceramic PIC181, Adv. Eng. Mater. **21**, 1900159 (2019).

[14] M. Hinterstein, M. Hoelzel, J. Rouquette, J. Haines, J. Glaum, H. Kungl, and M. Hoffman, Interplay of strain mechanisms in morphotropic piezoceramics, Acta Mater. **94**, 319 (2015).

[15] B. Noheda, D. E. Cox, G. Shirane, J. A. Gonzalo, L. E. Cross, and S.-E. Park, A monoclinic ferroelectric phase in the $PbZr_{1-x}Ti_xO_3$ solid solution, Appl. Phys. Lett. **74**, 2059 (1999).

[16] M. Hinterstein, K. A. Schoenau, J. Kling, H. Fuess, M. Knapp, H. Kungl, and M. J. Hoffmann, Influence of lanthanum doping on the morphotropic phase boundary of lead zirconate titanate, J. Appl. Phys. **108**, 24110 (2010).

[17] Y. Wang, Diffraction theory of nanotwin superlattices with low symmetry phase: Application to rhombohedral nanotwins and monoclinic MA and MB phases, Phys. Rev. B **76**, 024108 (2007).

[18] M. Hinterstein, H. E. Mgbemere, M. Hoelzel, W. Rheinheimer, E. Adabifiroozjaei, P. Koshy, C. C. Sorrell, and M. Hoffman, Influence of microstructure on symmetry determination of piezoceramics, J. Appl. Crystallogr. **51**, 670 (2018).

[19] A. Schökel *et al.*, Multi-Analyser detector (MAD) for high-resolution and high-energy powder X-Ray diffraction, J. Synch. Radiat. **28**, 146 (2021).

[20] J. E. Daniels, T. R. Finlayson, A. J. Studer, M. Hoffman, and J. L. Jones, Time-resolved diffraction measurements of electric-field-induced strain in tetragonal lead zirconate titanate, J. Appl. Phys. **101**, 94104 (2007).

[21] J. E. Daniels, C. Cozzan, S. Ukritnukun, G. Tutuncu, J. Andrieux, J. Glaum, C. Dosch, W. Jo, and J. L. Jones, Two-step polarization reversal in biased ferroelectrics, J. Appl. Phys. **115**, 224104 (2014).

[22] H. Choe *et al.*, Combining high time and angular resolutions: time-resolved x-ray powder diffraction using a multi-channel analyser detector, J. Appl. Crystallogr. **48**, 970 (2015).

[23] S. Gorfman, Sub-microsecond x-ray crystallography: Techniques, challenges, and applications for materials science, Crystallogr. Rev. **20**, 210 (2014).

[24] S. Gorfman, H. Simons, T. Iamsasri, S. Prasertpalichat, D. P. Cann, H. Choe, U. Pietsch, Y. Watier, and J. L. Jones, Simultaneous resonant x-ray diffraction measurement of polarization inversion and lattice strain in, polycrystalline ferroelectrics, Sci. Rep. **6**, 20829 (2016).

[25] K.-Y. Lee, X. Shi, N. Kumar, M. Hoffman, M. Etter, S. Checchia, J. Winter, L. Lemos da Silva, D. Seifert, and M. Hinterstein, Electric-field-induced phase transformation and frequency-dependent behavior of bismuth sodium titanate–barium titanate, Materials (Basel) **13**, 1054 (2020).

[26] K.-Y. Lee, X. Shi, N. Kumar, M. Hoffman, M. Etter, J. Winter, L. Lemos da Silva, D. Seifert, and M. Hinterstein, The complex structural mechanisms behind strain curves in bismuth sodium titanate–barium titanate, Appl. Phys. Lett. **116**, 182902 (2020).

[27] M. Herklotz, F. Scheiba, M. Hinterstein, K. Nikolowski, M. Knapp, A.-C. Dippel, L. Giebeler, J. Eckert, and H. Ehrenberg, Advances in in situ powder diffraction of battery materials: A case study of the new beamline P02.1 at DESY, hamburg, J. Appl. Crystallogr. **46**, 1117 (2013).

[28] H. Simons, J. E. Daniels, A. J. Studer, J. L. Jones, and M. Hoffman, Measurement and analysis of field-induced crystallographic texture using curved position-sensitive diffraction detectors, J. Electroceramics **32**, 283 (2014).

[29] P. Kraft *et al.*, Characterization and calibration of PILATUS detectors, IEEE Trans. Nucl. Sci. **56**, 758 (2009).

[30] M. Hoelzel, A. Senyshyn, N. Juenke, H. Boysen, W. Schmahl, and H. Fuess, High-resolution neutron powder diffractometer SPODI at research reactor FRM II, Nucl. Instrum. Methods Phys. Res. Sect. **667**, 32 (2012).

[31] B. Schmitt, C. Brönnimann, E. Eikenberry, F. Gozzo, C. Hörmann, R. Horisberger, and B. D. Patterson, Mythen Detector System, Nucl. Instrum. Methods Phys. Res. Sect. A **501**, 267 (2003).

[32] C. Dejoie, M. Coduri, S. Petitdemange, C. Giacobbe, E. Covacci, O. Grimaldi, P.-O. Autran, M. W. Mogodi, D. Šišak Jung, and A. N. Fitch, Combining a nine-crystal multi-analyser stage with a two-dimensional detector for high-resolution powder X-Ray diffraction, J. Appl. Crystallogr. **51**, 1721 (2018).

[33] I. Peral, J. McKinlay, M. Knapp, and S. Ferrer, Design and construction of multicrystal analyser detectors using rowland circles: Application to MAD26 at ALBA, J. Synch. Radiat. **18**, 842 (2011).

[34] A. B. Kounga, T. Granzow, E. Aulbach, M. Hinterstein, and J. Rödel, High-Temperature Poling of Ferroelectrics, J. Appl. Phys. **104**, 024116 (2008).

[35] A. J. Studer, M. E. Hagen, and T. J. Noakes, Wombat: The high-intensity powder diffractometer at the OPAL reactor, Phys. B Condens. Matter **385–386**, 1013 (2006).

[36] S. Matthies, J. Pehl, H. R. Wenk, L. Lutterotti, and S. C. Vogel, Quantitative texture analysis with the HIPPO neutron TOF diffractometer, J. Appl. Crystallogr. **38**, 462 (2005).

[37] D. A. Hall, A. Steuwer, B. Cherdhirunkorn, T. Mori, and P. J. Withers, A high energy synchrotron x-ray study of crystallographic texture and lattice strain in soft lead zirconate titanate ceramics, J. Appl. Phys. **96**, 4245 (2004).

[38] D. Bremecker, A. Wohninsland, S. Teuber, K. V. Lalitha, M. Hinter-stein, and J. Rödel, Texture-based ferroelectric hardening in $Na_{1/2}Bi_{1/2}TiO_3$-based piezoceramics, Acta Mater. (unpublished).

[39] N. Uchida and T. Ikeda, Electrostriction in perovskite-type ferroelectric ceramics, Jpn. J. Appl. Phys. **6**, 1079 (1967).

[40] M. Hinterstein, M. Knapp, M. Hoelzel, W. Jo, A. Cervellino, H. Ehrenberg, and H. Fuess, Field-induced phase transition in $Bi_{1/2}Na_{1/2}TiO_3$−based lead-free piezoelectric ceramics, J. Appl. Crystallogr. **43**, 1314 (2010).